Multiscale fatigue damage characterization in short glass fiber reinforced polyamide-66

M.F. Arif [a], N. Saintier [b,*], F. Meraghni [a], J. Fitoussi [c], Y. Chemisky [a], G. Robert [d]

[a] Arts et Métiers ParisTech, LEM3 – UMR CNRS 7239, 4 Rue Augustin Fresnel, 57078 Metz, France
[b] Arts et Métiers ParisTech, I2M – UMR CNRS 5295, Esplanade des Arts et Métiers, 33405 Talence, France
[c] Arts et Métiers ParisTech, PIMM – UMR CNRS 8006, 151 Boulevard de l'Hôpital, 75013 Paris, France
[d] Solvay Engineering Plastics, Avenue Ramboz BP 64, 69192 Saint-Fons, France

Keywords:
A: Polymer–matrix composites (PMCs)
B: Fatigue
B: Microstructures
E: Injection molding
Micro-computed tomography

A B S T R A C T

This paper aims at studying fatigue damage behavior of injection molded 30 wt% short glass fiber reinforced polyamide-66 composite (PA66/GF30). The evolution of dynamic modulus, hysteresis area, cyclic creep and temperature during fatigue tests were analyzed and discussed. Damage analyses by X-ray micro-computed tomography (μCT) technique on interrupted fatigue tests at several percentages of total fatigue life were performed to further understand the damage mechanisms and evolution during fatigue loading. It can be observed that experimental results related to the evolution of dynamic modulus, strain, temperature and energy dissipation are important and consistently complement each other for damage evaluation of PA66/GF30. During fatigue loading, diffuse damage occurs over the entire specimen though the damage does not necessarily exhibit the same level between different locations inside the specimen. The μCT analysis of voids characteristics demonstrates that the damage continuously increases during fatigue loading. The damage is developed notably along fiber interface in the form of fiber/matrix interfacial debonding.

1. Introduction

The reduction of vehicle mass is a major concern for automotive industries to comply with the strict pollution regulation, particularly for the CO_2 emission. Short fiber reinforced thermoplastic materials, among them is the short glass fiber reinforced polyamide-66, are good candidates to provide a compromise between the required lightweight and the expected thermomechanical performances. However, their structural durability has not yet been fully investigated. In particular further work to investigate the fatigue behavior of these composites is necessary to provide physically based damage mechanisms scenarios for fatigue modeling.

Various techniques have been used to evaluate the damage in short fiber reinforced thermoplastics. Early works of Horst and Spoormaker [1,2] performed fractography analysis onto the fracture surface of fatigue loaded short glass fiber reinforced polyamides by scanning electron microscopy (SEM) and they proposed a damage mechanisms scenario which consider that the damage starts at fiber ends and then propagates along fiber interface. The evolution of dynamic modulus, i.e. the slope of stress–strain hysteresis curve, has been proposed by several authors to evaluate the damage level of the composites [3–8]. Since the damage process is thermally activated and, in the same time, a dissipative process by nature, thermography technique by using infra-red camera has become an important tool for fatigue damage evaluation in composites [9–14]. Finally, due to the complex nature of the microstructure, damage is spatially distributed so that X-ray micro-computed tomography (μCT) technique has become a suitable and efficient tool for fatigue damage characterization in composite materials [15–17]. The work of Cosmi and Bernasconi [18] presents the potential and critical aspects of using μCT technique for fatigue damage characterization in short glass fiber reinforced polyamides. The current work is the continuation of the recently published work on damage characterization of PA66/GF30 under quasi-static loading by SEM and μCT techniques [19].

During fatigue loading of the composite, several phenomena may develop concurrently, such as damage, cyclic creep and increase of temperature. All of them may contribute to the overall fatigue strength of the material [20,21]. A comprehensive study of fatigue damage behavior is necessarily a coupled analysis of all interrelating phenomena during fatigue loading. The objective of this work is to characterize fatigue damage mechanisms of PA66/GF30 under uniaxial constant amplitude loading. It is proposed

* Corresponding author. Tel.: +33 556 845 361; fax: +33 556 845 366.
E-mail address: nicolas.saintier@ensam.eu (N. Saintier).

to use a combined analysis of dynamic modulus, cyclic creep, dissipated energy and temperature evolution during fatigue testing together with post-mortem 3D damage analysis by μCT to further understand the damage mechanisms of PA66/GF30 during fatigue testing. To evaluate the process induced anisotropy, two directions, longitudinal and transverse to the mold flow direction (MFD), are examined. In addition, a particular attention is given to the effect of skin–shell–core formation on the damage mechanisms of PA66/GF30. In fact, this type of microstructure is commonly observed in the injection molded short glass fiber reinforced polyamides [22–25]. The experimental results allow to analyze the importance of damage and their interrelated phenomena to the overall behavior of PA66/GF30, as well as to the identification of damage mechanisms and evolution.

In summary, the organization of this work is as follows: Section 2 presents material and process induced microstructure description, followed by the specimens used for mechanical characterization in Section 3. In Section 4, the experimental procedures and damage investigation techniques are detailed. In Section 5, the results of microscopic and macroscopic damage analysis of PA66/GF30 are discussed. Afterwards, the damage characteristics and all the contributing factors to the overall fatigue strength, as well as the damage mechanisms chronology of PA66/GF30 are concluded in Section 6.

2. Material and process induced microstructure description

The material studied is a 30 wt% short glass fiber reinforced polyamide-66 composite (PA66/GF30) provided by Solvay Engineering Plastics-France, under the commercial name of Technyl® A218V30. The material was prepared by compounding the polyamide-66 pellets and chopped short glass fibers in a twin-screw extruder. Subsequently, PA66/GF30 compound was transferred into an injection molding machine, resulting in $360 \times 100 \times 3.2$ mm^3 of rectangular plate.

It is commonly established through open literature [22–25] that fiber orientation distribution is widely governed by injection process. In fact, for a system where polymer melt flows through a small cavity between two parallel walls, shear flow has maximum value near to the mold wall whereas it vanishes at the core zone. This leads the fibers to be oriented parallel (and perpendicular) to MFD at the shell (and core) layers. Moreover, a thin random skin layer can be formed due to the polymer melt that is in direct contact with a relatively cold mold wall temperature.

X-ray micro-computed tomography (μCT) technique was employed to study the microstructure heterogeneity of PA66/GF30 in terms of its fiber orientation. The μCT experiment was carried out at ID19 beam line of the European Synchrotron Radiation Facility (ESRF) Grenoble, France [26]. For this microstructure investigation, the experimental setup was conditioned to reach a voxel resolution of 1.4 μm. Two samples for μCT experiments were extracted from the injection molding plate at two positions along mold flow direction (MFD) axis, as shown in Fig. 1. The selected positions were significantly far from the complex flow zones at the initial and final filling stages. Indeed, nonuniform microstructure is usually found at these complex flow zones. Moreover, the selected positions were also used as a guideline for specimens extraction for the tensile and fatigue tests that will be discussed in Section 3. The dimensions of the μCT samples were $2 \times 2 \times 3.2$ mm^3, where 3.2 mm corresponds to the sample thickness. The μCT scanning was not carried out through all the sample thickness but it always covered more than half of the thickness so that the skin–shell–core structure can always be captured.

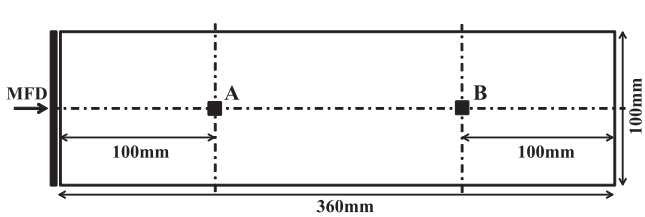

Fig. 1. Locations of μCT sample extraction for injection molding induced microstructure investigation (A and B).

The microstructure of PA66/GF30 obtained from the μCT sample extracted from position A of Fig. 1 is shown in Fig. 2. It can be seen from Fig. 2, PA66/GF30 has a specific injection molding process induced microstructure characterized by a skin–shell–core structure. Moreover, transition layers between shell and core are also observed. The microstructure of PA66/GF30 extracted from position B exhibits qualitatively the same trend as the one extracted from position A. This microscopic condition was achieved by an optimal set up of injection molding parameters (barrel and mold temperatures, injection speed, etc.) to ensure a high compaction degree of PA66/GF30 and to reduce the core layer thickness.

To acquire the real tendency of fiber orientation throughout the samples, the tensor representation of fiber orientation state proposed by Advani and Tucker [27] is used in this work. This method is widely used to characterize the fiber orientation due to its efficiency, simplicity and relatively short computational time. The complete review of this method can be found elsewhere [28–30]. A strategic method of μCT 3D image segmentation of the fibers via gray level thresholding has been developed to capture efficiently the Euler orientation angles of the fibers. Avizo and Visilog softwares were used for this purpose. The second-order fiber orientation tensors have been computed based on the data of fibers' Euler angles. The normalized first tensor components (a_{11}) of the two studied μCT volumes are shown in Fig. 3. The a_{11} tensor component represents the degree of fibers to orient longitudinal (parallel) with respect to the MFD. Higher value of a_{11} constitutes higher tendency of fibers to orient to the MFD. It can be seen from Fig. 3 that the skin–shell–core layers of the two μCT samples are well-defined. In addition, small transition regions between the shell and core layers are also observed.

Based on the qualitative and quantitative analysis by μCT, it can be seen that the skin layers, the upper and lower specimen surfaces, are slightly random in fiber orientation. However, the orientation tensor (Fig. 3) shows that the principal fiber orientation in the skin layer tends to follow the MFD. The shell layers are the most dominant ones with preferential fiber orientation longitudinal to the MFD. Thin core layer is developed and mostly fibers in this layer are oriented transversely to the MFD. It is worth noting that instead of purely oriented transversely to the MFD, it has been frequently observed that fibers in the core layer are slightly tilted around 5–20° from the transverse direction, such as the one shown in Fig. 2d. In addition to the skin, shell and core microstructures, transition layers between shell and core are also observed, as shown in Figs. 2c and 3.

The normalized orientation tensors of the two studied samples show that both positions exhibit almost the same state of fiber orientations. Only small differences on the width of the shell–core transition zones and the orientation state of the skin layers are observed between the two studied samples. It can be inferred from the results that the microstructure developed along the MFD axis of the injection molding plate is generally homogeneous.

3. Specimen

Specimens used for mechanical tests were machined from the rectangular plate produced by injection molding. To consider the

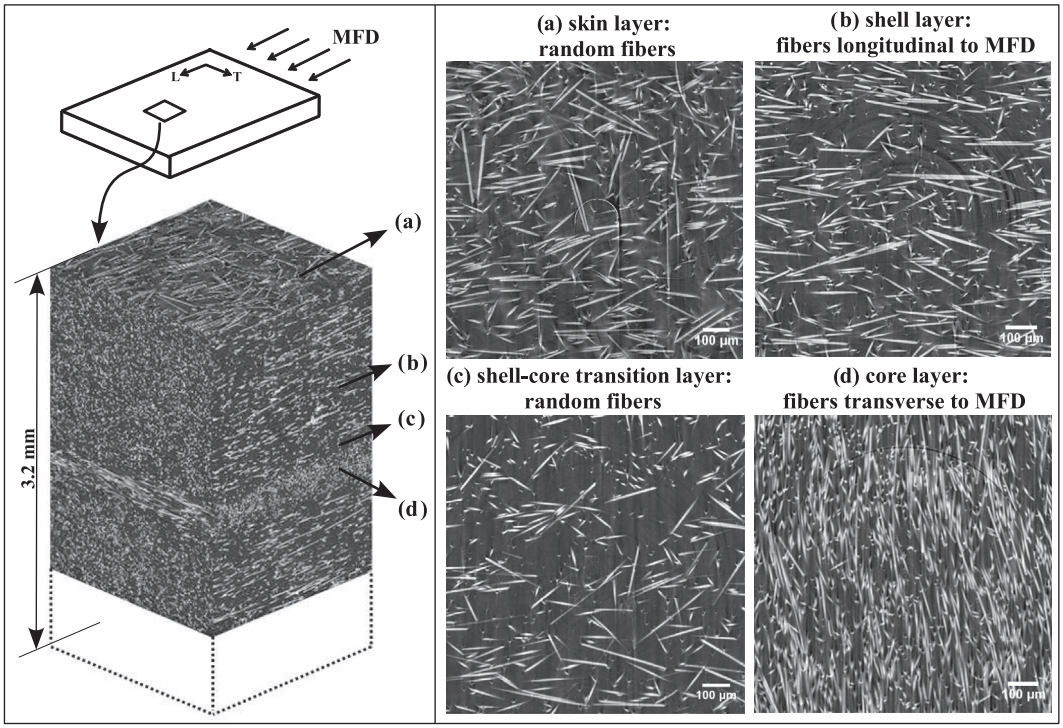

Fig. 2. Skin–shell–transition–core microstructure formation of PA66/GF30 observed by μCT technique.

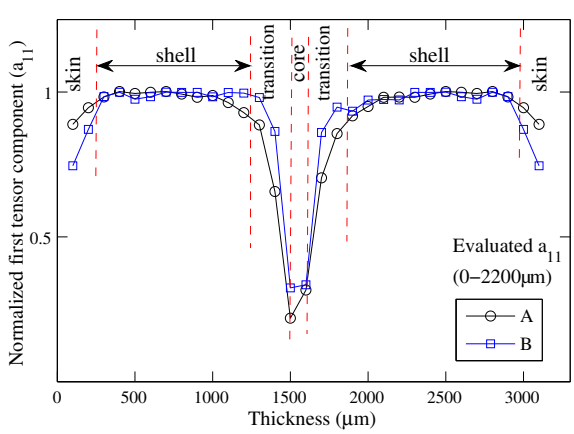

Fig. 3. Normalized first tensor component (a_{11}) of the two studied samples. The a_{11} is evaluated from 0 to 2200 µm thickness. The a_{11} above 2200 µm is assumed to be symmetric with another half of the thickness.

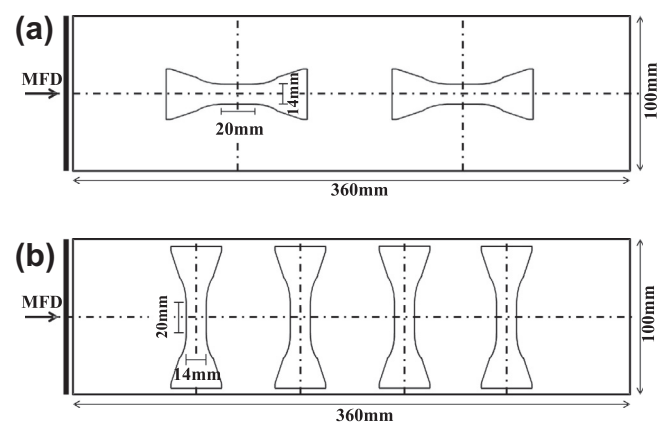

Fig. 4. Machining locations of (a) longitudinal and (b) transverse specimens, as well as the main specimen dimensions of PA66/GF30.

anisotropy effect induced by the skin–shell–transition–core structure of the composite, the specimens were machined in longitudinal and transverse directions with respect to the MFD, defined hereafter as *the longitudinal and transverse specimens*. The longitudinal and transverse specimens were machined from several positions of the injection molding plate as shown in Fig. 4. To ensure microstructure homogeneity between all specimens, the specimen extraction locations were chosen far from the injection gate and end-filling zones. Moreover, the specimen gauge-length zones were assured to be along the MFD axis. As discussed earlier, the microstructure developed along the MFD axis of the injection molding plate is generally homogeneous. The machining positions of the longitudinal and transverse specimens, as well as the specimen main dimensions are presented in Fig. 4. During mechanical tests, the longitudinal and transverse specimens were selected randomly from these locations.

4. Experimental procedures and damage investigation techniques

Tensile and fatigue tests were performed on dry as molded PA66/GF30 (<0.2% water content) at room temperature. Quasi-static tensile tests were performed upon a servo-hydraulic machine at a crosshead speed of 1 mm/min, which corresponds to the strain rate of 3×10^{-4} s^{-1}. Fatigue tests were performed by applying a sinusoidal signal, under load controlled mode, at constant amplitude and fixed loading ratio. To prevent specimens from buckling, the fatigue tests were conducted under tension–tension mode, with a stress ratio of $R = \sigma_{min}/\sigma_{max} = 0.1$. The frequency of 3 Hz was chosen in order to avoid a global heat of the sample reaching the glass transition of dry PA66/GF30 (≈65–70 °C) during fatigue loading. Fatigue strength of the material was evaluated within the range of 10^3–10^6 cycles. Continuous temperature monitoring of the active zone of the specimen was assured by the CEDIP Jade

III MWR infrared camera with a spectral range between 3.9 and 4.5 μm.

Damage mechanisms and its evolution were investigated by the use of μCT analyses performed on longitudinal and transverse specimens after being subjected to fatigue loading up to several percentages of total fatigue life. For this damage investigation, the μCT experimental setup was conditioned to reach voxel resolutions of 0.7 and 1.4 μm. The longitudinal specimens were consistently carried out at 0.7 μm resolution, whereas the transverse specimens were employed at 1.4 μm resolution. Both resolutions demonstrated consistent results though the ones with 0.7 μm provided stronger physical interpretations. The μCT sample dimensions for this damage investigation were the same as the ones for the microstructure analysis previously discussed in Section 2. The μCT samples were machined from the central gauge-length zone of the fatigue loaded specimens. For the specimens that have been fatigue loaded up to failure, the extraction locations of the μCT samples were far from the fracture surface in order to avoid fast crack propagation effect due to the final failure. The μCT investigation on virgin sample was also carried out as a reference for the damage analysis of fatigue loaded specimens. By segmentation technique with proper and consistent selection of threshold value, the voids inside the analyzed μCT volume element can be isolated, thereby the void features such as volume, Euler orientation angles and aspect ratio can be quantified. The threshold level was defined and optimized based on visual observation of the voids at fatigue loaded specimens. All the specimens, including the virgin, were treated using similar and constant threshold level in order to allow a direct comparison between them. In this work, μCT images are presented to demonstrate the fatigue damage mechanisms of the composite. The void volume, aspect ratio and Euler orientation angles are also presented to confirm the damage mechanisms and evolution of PA66/GF30.

5. Experimental results and discussion

5.1. Overall material characteristics

5.1.1. Tensile properties

The tensile properties of PA66/GF30 are described in Fig. 5. This figure illustrates the strong anisotropy effect induced by the injection molding process. The Young modulus and ultimate stress of the longitudinal specimens are twice than the ones of the transverse specimens. Nevertheless, strain to failure characterizing the material ductility of the longitudinal specimens is half than that of the transverse specimens. The fiber orientations through the thickness of the specimens are predominantly occupied by the shell layer where the fibers are longitudinally oriented to the MFD. This yields the shell layer to dominantly govern the tensile behavior of PA66/GF30. Moreover, Fig. 5 illustrates different data scatter between longitudinal and transverse specimens. Transverse specimens demonstrate a much larger data dispersion than that in longitudinal specimens. This is probably due to the fiber orientation variability in the core layer. As previously discussed in Section 2, instead of exclusively oriented transversely to the MFD, tilted fibers around 5° to 20° from the transverse direction are frequently observed. Since the core layer in the transverse specimens is responsible for the load transfer mechanism due to its parallel orientation to the applied load direction, the core layer orientation variability may lead to a data scatter in the mechanical properties of the transverse specimens.

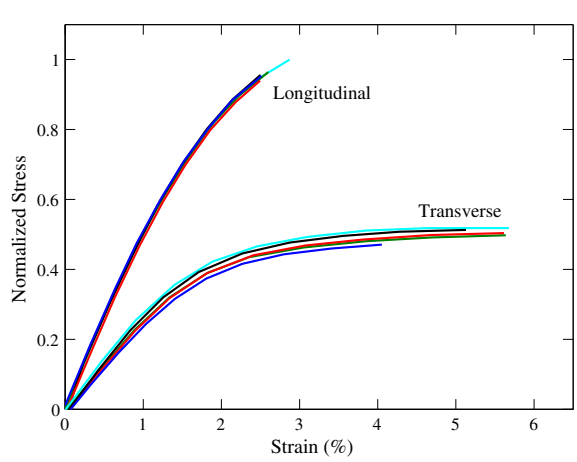

Fig. 5. Tensile properties of longitudinal and transverse specimens of PA66/GF30.

5.1.2. Strain rate evolution during fatigue test

The strain rate during fatigue loading can be estimated using the derivative of the strain equation. If one considers that the strain response of the composite follows a sinusoidal wave equation $\varepsilon(t) = \Delta\varepsilon \sin(\omega t) + \bar{\varepsilon}$, the strain rate will be $\dot{\varepsilon}(t) = \Delta\varepsilon\omega\cos(\omega t)$, where ε and $\dot{\varepsilon}$ are respectively the strain and strain rate (s^{-1}), $\Delta\varepsilon$ and $\bar{\varepsilon}$ are respectively the strain amplitude and mean strain, $\omega = 2\pi/T$ is the angular frequency (rad/s), T is the period (s) and t is the time (s). The description of these variables is given in Fig. 6.

According to the above-mentioned strain rate equation, the composite experiences a continuous change of strain rate during cyclic loading. The maximum strain rate during a cycle is given by $\dot{\varepsilon}_{max} = \Delta\varepsilon\omega$. Evaluating only the maximum value of strain rate, one can see from Fig. 7 that the strain rates in longitudinal and transverse specimens are ranging from 7×10^{-2} to 2×10^{-1} s^{-1} even though the maximum stress levels of both specimens are very different. The strain rates in all specimens are nearly constant during fatigue loading except the one of the transverse specimen loaded at the highest maximum stress level, which could be due to the high heat generation and thus higher viscous properties of PA66/GF30. It has to be noted that the range of the strain rate in the fatigue test of PA66/GF30 is significantly higher than that in the quasi-static tensile test. Tensile tests performed at a strain rate of about 10^{-1} s^{-1} led to a fracture before reaching the ultimate stress commonly achieved at quasi-static strain rates. For these reasons, fatigue load levels will be given by referring to the ultimate stress obtained from the quasi-static tensile tests.

5.1.3. Fatigue S–N curve

Fatigue life (S–N) curve of PA66/GF30 is reported in Fig. 8. In line with the results of quasi-static tensile tests, the fatigue strength of longitudinal specimens are about twice higher than that of transverse specimens. It is also shown that the S–N curves

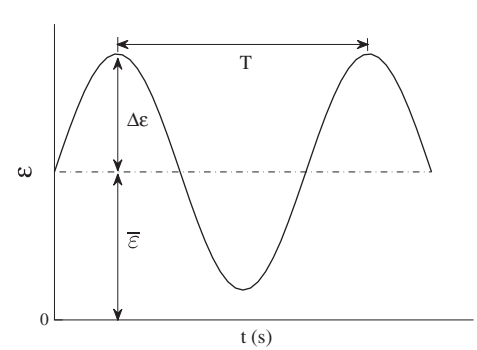

Fig. 6. Schematic of sinusoidal wave form of strain response of material under fatigue loading.

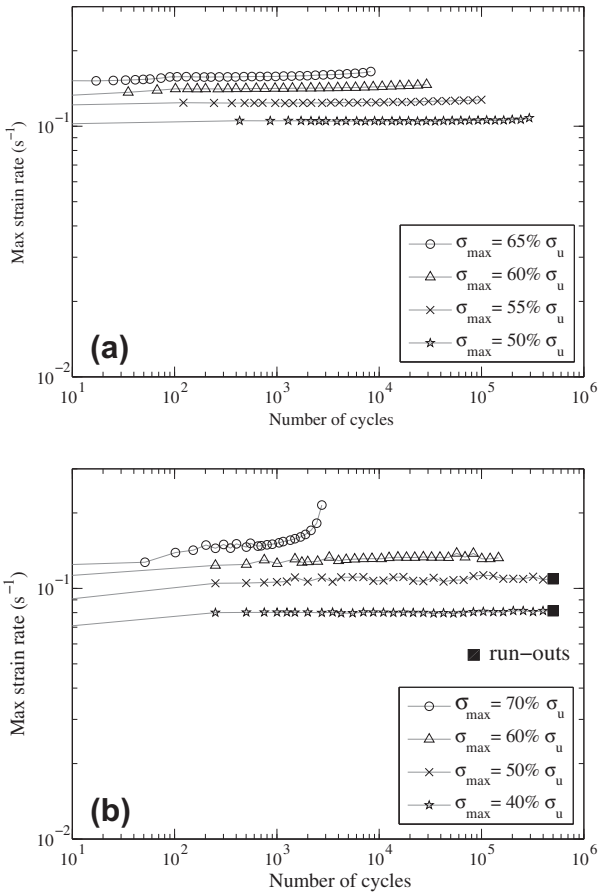

Fig. 7. Evolution of maximum strain rate of (a) longitudinal and (b) transverse specimens during fatigue loading of PA66/GF30. (σ_u represents the ultimate tensile strength of its respective orientation angles).

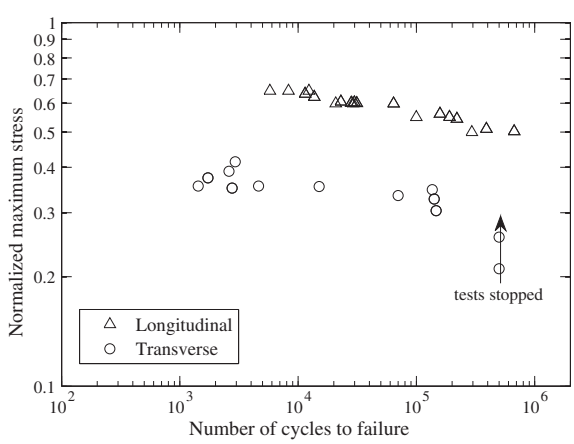

Fig. 8. The *S–N* curves of longitudinal and transverse specimens. Maximum stresses are normalized with the ultimate tensile strength of longitudinal specimen.

are linear in terms of maximum stress vs. number of cycles in a log–log representation. The current result is consistent with the previously published work in short glass fiber reinforced polyamides [22,31,32]. It is worth noting that for the low stress levels of transverse specimens, the fatigue tests were stopped if the specimens did not reach final failure at 5×10^5 cycles. Stopping the fatigue tests at 5×10^5 cycles was a compromise that allow the tests to be performed in a reasonable time with significant evolution of the observable variables. However it does not mean that a fatigue endurance limit has been reached at those stress levels and that no damage occurs below the corresponding stress levels. According to the published works on fatigue behavior of short glass fiber reinforced polyamides, one cannot reach a distinctive endurance limit stress up to 10^6 cycles [1,20,31], or even up to 10^7 cycles [32,33].

5.2. Macroscopic damage evaluation

5.2.1. Thermo-elasto-visco-damage coupling

Fig. 9 illustrates the evolution of the monitored parameters, i.e. normalized dynamic modulus (E_N/E_0), maximum strain (ε_{max}) and mean temperature ($T_{mean} - T_{room}$) for the longitudinal and transverse specimens. During cyclic loading, energy dissipation can be associated to different phenomena such as damage development and intrinsic dissipation (viscous behavior). Part of the mechanical strain energy due to the damage development and viscous effect of the material is turned into heat so that thermo-elasto-visco-damage coupling can occur during fatigue loading.

The dynamic modulus reduction can be used as a damage indicator when considering a classical continuum damage mechanics framework [6,34]. For all loading cases encountered in this study, the normalized dynamic modulus evolution demonstrates a stable value for the first 10^3 cycles and then decreases at a rate that depends on the loading level. In all cases, the intensity of the decrease of the normalized dynamic modulus is directly related to the fatigue life of the specimen.

The evolution of mean temperature exhibits two regimes (Fig. 9). The first one corresponds to a stable normalized modulus, where heat dissipation seems to be mostly related to the intrinsic energy dissipation associated to the viscous nature of the composite. The second regime is associated to the onset of the decrease of the normalized dynamic modulus and it corresponds to an inflection point on the mean temperature evolution. This regime change can be associated to the fact that the strain energy is not only dissipated into heat due to the viscous nature of the composite but also dissipated into a damage development and accumulation.

As shown in Fig. 9, the maximum strain continuously increases during fatigue life. The minimum strain exhibits the same trend (Fig. 10) so that the strain amplitude is almost constant during fatigue loading. It can then be stated that the observed damage is associated to a combined effect of creep and cyclic loading. However, since the mean strain evolution is maintained in reasonable ranges for most of the fatigue tests (lower than 1%), and that the dynamic modulus reduction is not associated to a change in the mean strain evolution, which could indicate an acceleration of the creep damage, it is believed that most the observed damage is related to the cyclic component of the loading and that the creep damage is limited for these dry as molded specimens. The situation is different for the transverse specimen loaded at the highest maximum stress level. At such high stress level, thermal softening is considered to arise as revealed by the significant increase of the maximum strain at the end of the fatigue life. It is also found a small evolution of dissipated strain energy during the fatigue tests and the decrease in the dynamic modulus is not associated to a significant modification in the intrinsic dissipation characteristics of the material (Fig. 11). Therefore, it can be inferred that the dynamic modulus reduction is related to a high extent to the damage evolution, except for the highest loading level of the transverse specimen ($\sigma_{max} = 70\%\sigma_u$) where thermal softening may occur and would lead to the final failure.

The longitudinal and transverse specimens exhibit different behavior considering that the thermo-elasto-visco-damage coupling in longitudinal specimens is higher than that in transverse specimens. With the stress levels significantly lower than those in longitudinal specimens, the transverse specimens generate higher changes in dynamic modulus, strain and temperature. This

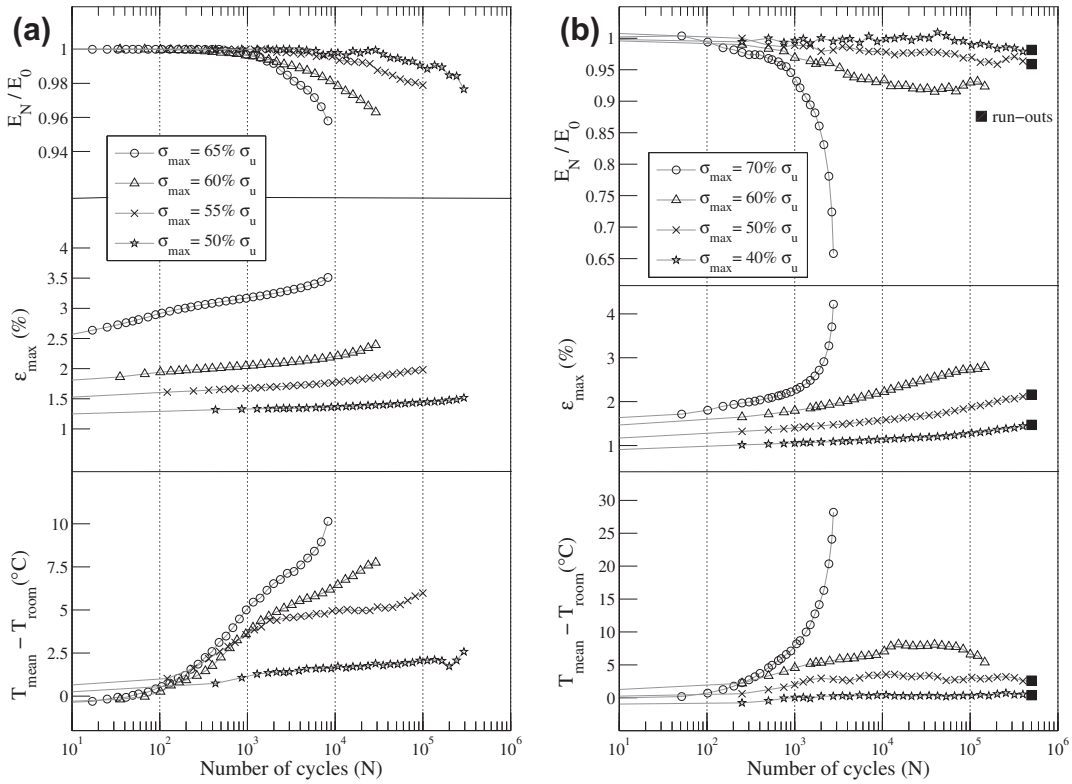

Fig. 9. Evolution of normalized dynamic modulus (E_N/E_0), maximum strain (ε_{max}) and mean temperature ($T_{mean} - T_{room}$) of (a) longitudinal and (b) transverse specimens during fatigue loading of PA66/GF30. (σ_u represents the ultimate tensile strength of its respective orientation angles).

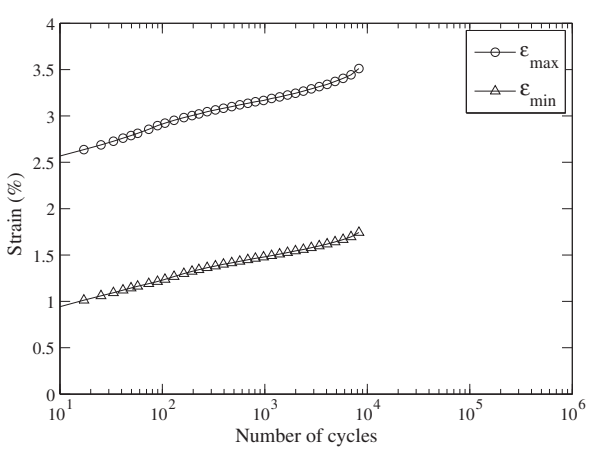

Fig. 10. Evolution of maximum and minimum strain of longitudinal specimen fatigue loaded at maximum stress of 65% σ_u. All loading cases encountered in this study exhibit similar trend as ε_{min} follows ε_{max} at approximately a constant offset.

is due to the fact that in transverse specimens, the polyamide-66 matrix has a more important role than that of fibers during the fatigue loading.

It can be summarized that the information of dynamic modulus is important though it becomes more difficult to completely comprehend the fatigue damage behavior without the information of strain, temperature and dissipated energy evolution. The evolution of dynamic modulus can be considered as a damage indicator. However for high stress levels, it may overpredict the damage evolution due to the high viscous effect contribution of the composite, such as the one shown in the highest loading level of the transverse specimen. Therefore, the spatial distribution analysis of damage and the microstructural investigation of damage mechanisms by μCT are necessary to further understand the fatigue damage in PA66/GF30.

5.2.2. Spatial distribution of damage

In a material discontinuity such as damage, heat transfer is hindered since there is only partial or no contact between the internal surfaces of the damage zone. This could result in a local increase of temperature in the damage zone. If one records the mean and maximum temperature on the active zone area of the specimen, it is expected that the temporal increase of the maximum temperature will be higher than that of the mean temperature when a localized damage is detected. However, the nature of this technique suggests that the level of localized damage should be high enough so that the heat generated in the damage zones can reach the surface and thus can be captured by the infrared thermography camera.

This experimental approach has been examined in PA66/GF30 specimens. As described in Fig. 12, the maximum temperature evolution follows that of the mean temperature, with approximately a constant offset. This result indicates that during fatigue loading, there is no macroscopic damage induced strain localization and the damage is preferably diffused over the entire specimen. An increase of maximum temperature is only observed when the number of cycles reaches 99% of fatigue life. This is due to the sudden crack propagation leading to the final fracture of the sample.

5.3. Microscopic damage evaluation

The μCT is a powerful 3D non-destructive investigation method to analyze microscopic characteristics of a medium. By applying 3D reconstruction, fibers in a composite can be observed and further post-processed to obtain their features such as volume, aspect ratio and orientation angles. Also, voids that are the characteristic of damage can be observed and quantified. Indeed, in fatigue loaded

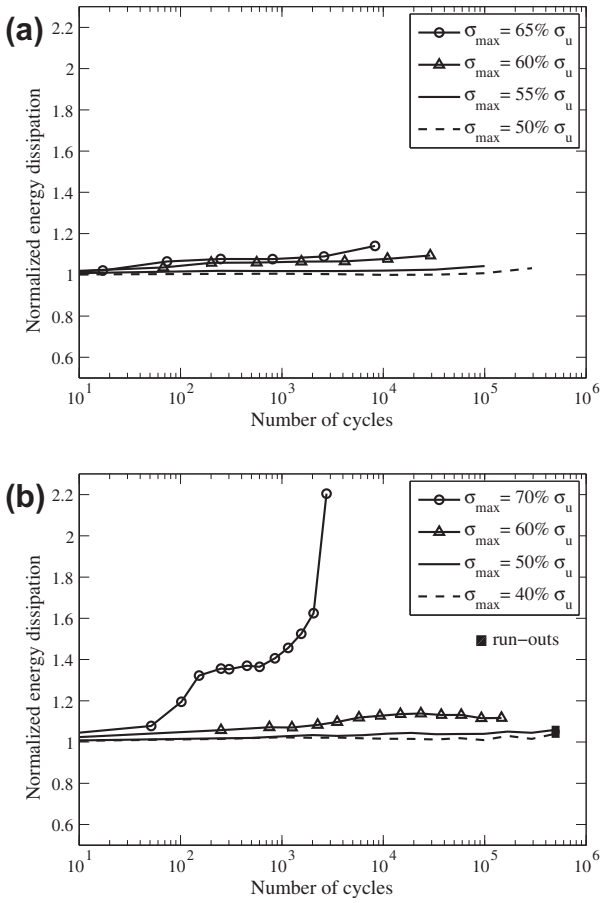

Fig. 11. Evolution of normalized energy dissipation of (a) longitudinal and (b) transverse specimens during fatigue loading of PA66/GF30. The energy dissipation was obtained by evaluating the hysteresis area at each loading cycle normalized by the initial value.

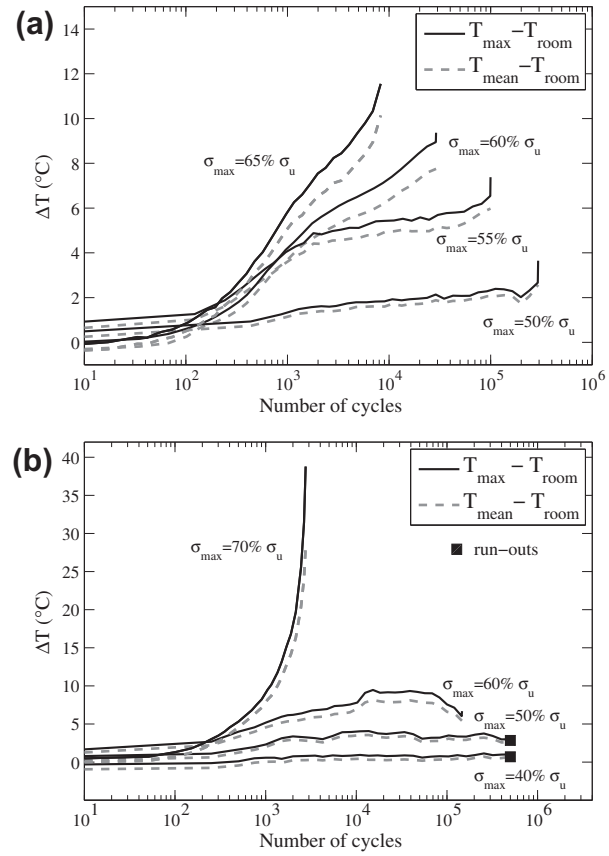

Fig. 12. Evolution of mean and maximum temperature of (a) longitudinal and (b) transverse specimens during fatigue loading of PA66/GF30.

specimens of PA66/GF30, the appearing of zones darker than the matrix is the characteristic of voids. By comparison with virgin specimen, the presence of these dark zones can be associated to fatigue damage.

In virgin specimen, almost no visible damage is observed inside the sample, as shown in Fig. 13. Few zones darker than the matrix are observed in the virgin sample, which could be due to the real initial damage or due to the image artifact. In fatigue loaded specimens, these dark zones are frequently observed, notably along fiber interface. These zones correspond to the damage in the form of fiber/matrix interfacial debonding, as shown in Fig. 14. However, one cannot asses whether the local damage is adhesive or cohesive from this μCT investigation. Indeed, fiber/matrix interfacial debonding depends on several parameters, among them are relative humidity and fiber orientation. Voids at fiber ends are also observed in the fatigue loaded specimens, though it is not necessarily involved in the fiber/matrix interfacial debonding. Few fiber breakages are also observed but it seems this damage mechanism is not dominant. In a particular case, matrix microcracks can be developed, such as the one observed in the core layer of the transverse specimen (Fig. 15). The relatively thin core layer is believed to bear higher stress level due to its longitudinal (parallel) orientation to the applied load direction. Matrix microcracks, with preferential direction transversely to the applied load direction, as well as to the fibers direction, are found to develop favorably in this region.

Since the presence of the damage can be in the form of nanoscopic voids, visual demonstration by the original μCT radiographs is sometimes not sufficient. A further treatment after the segmentation process of μCT volumes has been carried out to allow a joint representation of the damage and fibers, each of them having different colors, and without the matrix on the final images. Fig. 16 shows an example of magnified image in a zone with highly debonded fibers. This fiber/matrix interfacial debonding is frequently

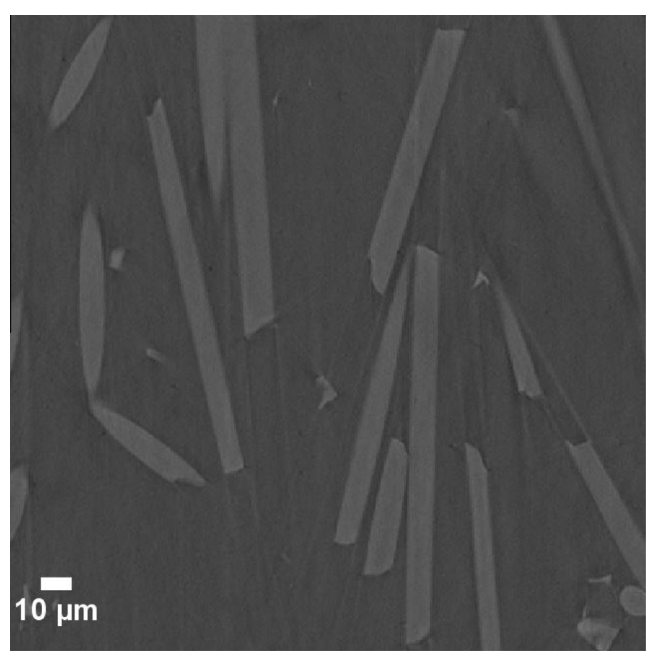

Fig. 13. The μCT image of virgin sample.

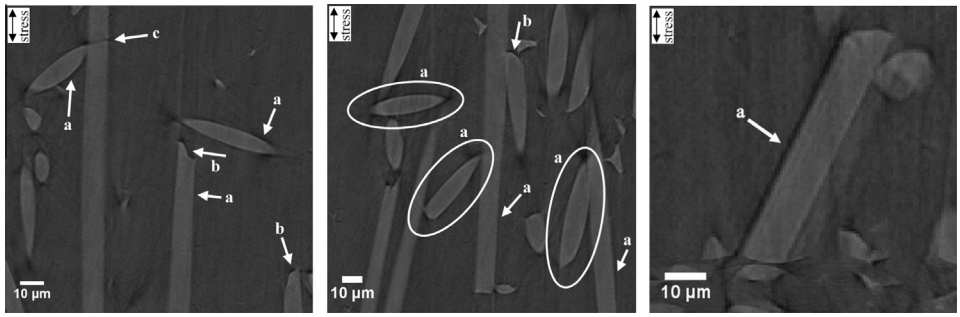

Fig. 14. Damage mechanisms observed in the shell zone of longitudinal specimen that has been fatigue loaded up to failure at maximum stress of 60% σ_u; (a) fiber/matrix interfacial debonding, (b) void at fiber ends, and (c) fiber breakage.

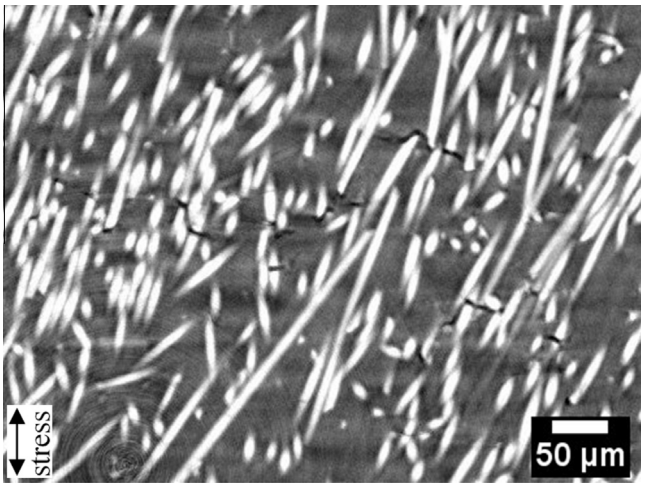

Fig. 15. Matrix microcracks observed at the core zone of transverse specimen that has been fatigue loaded up to failure at maximum stress of 60% σ_u.

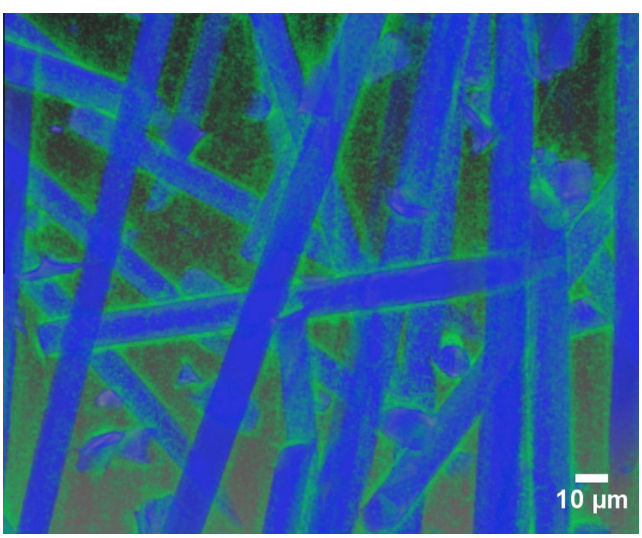

Fig. 16. A rendered μCT image of a zone with highly debonded fibers in the shell layer of longitudinal specimen that has been fatigue loaded up to failure at maximum stress of 60% σ_u. The blue and green colors represent the fiber and damaged zone, respectively. (For interpretation of the references to color in this figure legend, the reader is referred to the web version of this article.)

observed at the fatigue loaded specimens and can be considered as the main fatigue damage mechanism for PA66/GF30. In terms of spatial distribution of damage, though the damage is diffused over the entire specimen, the damage level between different locations inside the specimen is not necessarily the same (Fig. 17).

To propose a first attempt to quantify the damage and build a more consistent analysis on damage mechanisms of PA66/GF30, the void aspect ratio vs. void orientation angles are analyzed. To reduce the number of analyzed voids and to establish a consistent comparison between the void properties in the shell and core layers, the evaluation of void aspect ratio has been carried out in a 50 µm volume slice of the shell and core layers of the μCT volume, as described in Fig. 18. The μCT result of virgin specimen is given in Fig. 19 in the form of polar graph. For the virgin specimen, voids with low aspect ratio are observed in the shell layer. The trend in the core layer is the same as the one noticed in the shell layer. These small voids could be partly due to the real initial damage and partly due to the gray level fluctuation-induced inherent artifacts as a result of the thresholding technique. It should be noted that the thresholding technique was defined and optimized based on visual observation of voids in the fatigue loaded specimens. The chosen threshold level is unique and applied to all specimens, including the virgin sample. By this method, one can ensure that

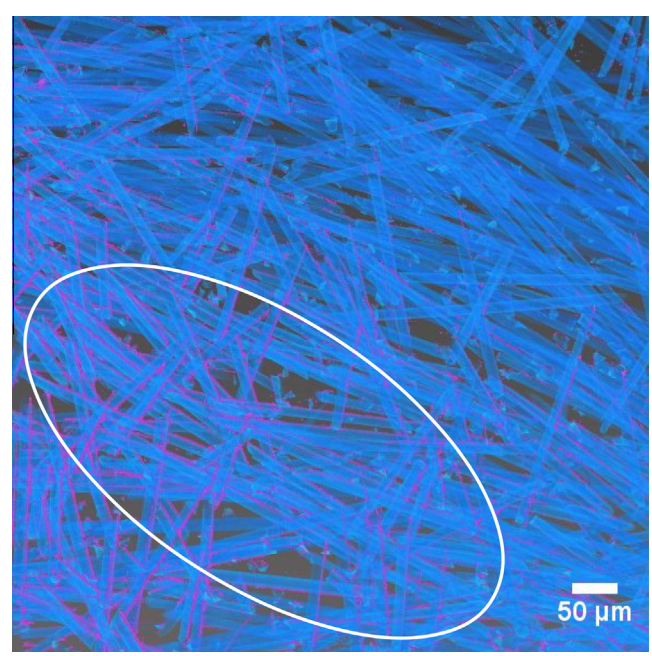

Fig. 17. A rendered μCT image which shows heterogeneous damage level at microscopic scale (the highlighted zone shows higher damage). The image was taken from longitudinal specimen that has been fatigue loaded up to 75% of fatigue life at maximum stress of 60% σ_u. The blue and magenta colors represent the fiber and damaged zone, respectively. (For interpretation of the references to color in this figure legend, the reader is referred to the web version of this article.)

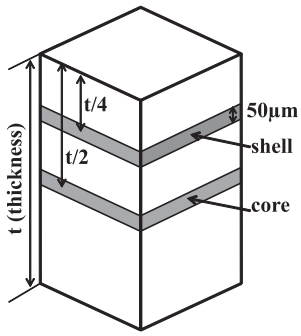

Fig. 18. Description of the analyzed μCT volumes in the shell and core regions of the composite.

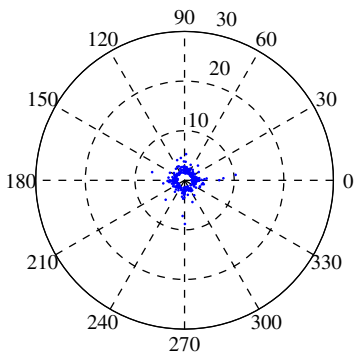

Fig. 19. Void aspect ratio vs. void orientation angle in the shell zone of virgin specimen.

any deviations of the subsequent void aspect ratio and volume analyses for the fatigue loaded specimens are not due to the thresholding technique but mostly related to the damage development.

Figs. 20 and 21 illustrate the void aspect ratio vs. angular position of longitudinal and transverse specimens, respectively, that have been fatigue loaded up to failure at maximum stress level of 60% σ_u. Significant damage is observed when comparing these results to the one of the virgin material (Fig. 19). In longitudinal specimen, the voids in the shell and core layers are mainly oriented at 0° and 90°, respectively (Fig. 20). It is worth noticing that these orientations are the same as the principal fiber orientations in the shell and core layers. It means the voids are mainly located along fiber interface in the form of fiber/matrix interfacial debonding. For the transverse specimen, the voids in the shell and core layers are both oriented at 90°, as shown in Fig. 21. It shows that fiber/matrix interfacial debondings occur in the shell layer, while matrix microcracks with preferential direction transversely to the applied load as well as to the fibers direction are dominant in the core layer of the composite. The random skin layers in the longitudinal and transverse specimens exhibit the same behavior as those in the shell layers. Even though the thin random skin layers are developed, the degree of random orientation is not high and the fibers in this layer tend to orient according to MFD, which is the same orientation as the ones in the shell layer (Fig. 3). For the transverse specimen, less fiber/matrix interfacial debonding is observed. Thi is probably due to the high development of matrix microcracks in addition to the fiber/matrix interfacial debonding as observed in the 2D images (Figs. 14 and 15). These figures illustrate clearly the anisotropic nature of the damage developed at the local scale.

In addition to the final stage damage investigation, similar μCT analyses were performed on longitudinal specimens that have been fatigue loaded up to several percentages of fatigue life. Fig. 22 illustrates the evolution of void volume as a function of void orientation and number of cycles at the shell layer of longitudinal specimens that have been fatigue loaded up to several percentages of fatigue life. It clearly shows that the void volumes increase throughout the fatigue life. It is worth noting that voids with low volumes are also observed in the virgin sample, which could be due to the real initial damage or fluctuation of the gray level. The majority of voids with high volume in the shell layers are oriented at 0°, longitudinal to the fiber orientation as well as to the applied load direction. This signifies that the voids, notably with high volumes, are located along fiber interface in the form of fiber/matrix interfacial debonding. These results are consistent with the aspect ratio analyses performed previously. In terms of evolution, the damage increase shows little evolution in the first 0–50%. However it evolves more significantly in the second half of the total fatigue life. It is important to notice that this evolution corresponds to the dynamic modulus evolution given in Fig. 9. If one considers the change in the total void volume ΔV with respect to the initial void volume, one can obtain that $\Delta V_{50\%N_f} < 0.5\%, \Delta V_{75\%N_f} = 1.3\%$ and $\Delta V_{100\%N_f} = 2.5\%$. This evolution agrees very well with the dynamic modulus evolution in the final stage. However the μCT analyses were not able to capture the damage evolution at the early stage of fatigue life. This is most probably due to the fact that opening of the interface above the resolution limit is needed to make it possible to be detected by the μCT analyses.

In terms of spatial distribution of the damage, based on the macroscopic characterization technique discussed in Section 5.2.2, the damage is preferentially diffused over the entire specimen. However, based on the microscopic observation by μCT technique, though the diffuse damage is observed, the damage level between different locations inside the specimen is not necessarily the same. Quantification of the local fiber density and its effects on the fiber/matrix interfacial debonding process is underway and will be the subject of a forthcoming paper.

Finally, it can be summarized that the observed voids can be associated in a large extent to the fiber/matrix interfacial debonding, complete or partial depending on the local configuration of the

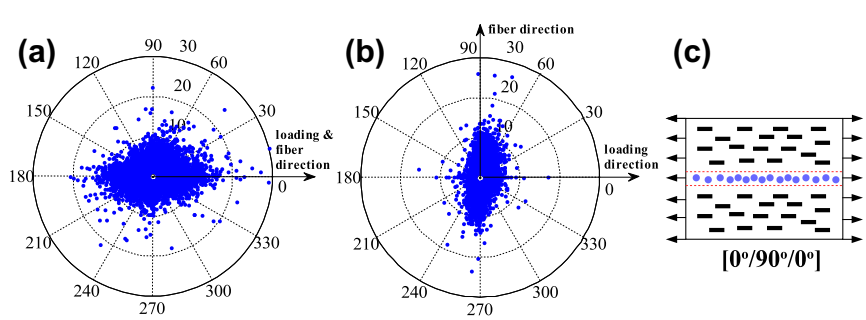

Fig. 20. Void aspect ratio vs. void orientation angle in (a) shell and (b) core regions of fatigue loaded longitudinal specimen. Laminate representation analogy of longitudinal specimen is presented in (c) for an interpretation guideline of void orientation angle.

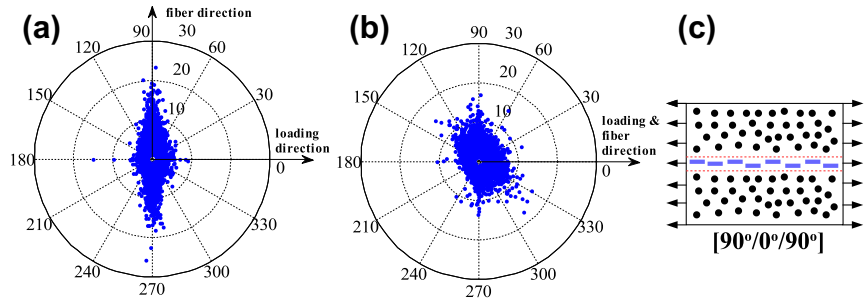

Fig. 21. Void aspect ratio vs. void orientation angle in (a) shell and (b) core regions of fatigue loaded transverse specimen. Laminate representation analogy of transverse specimen is presented in (c) for an interpretation guideline of void orientation angle.

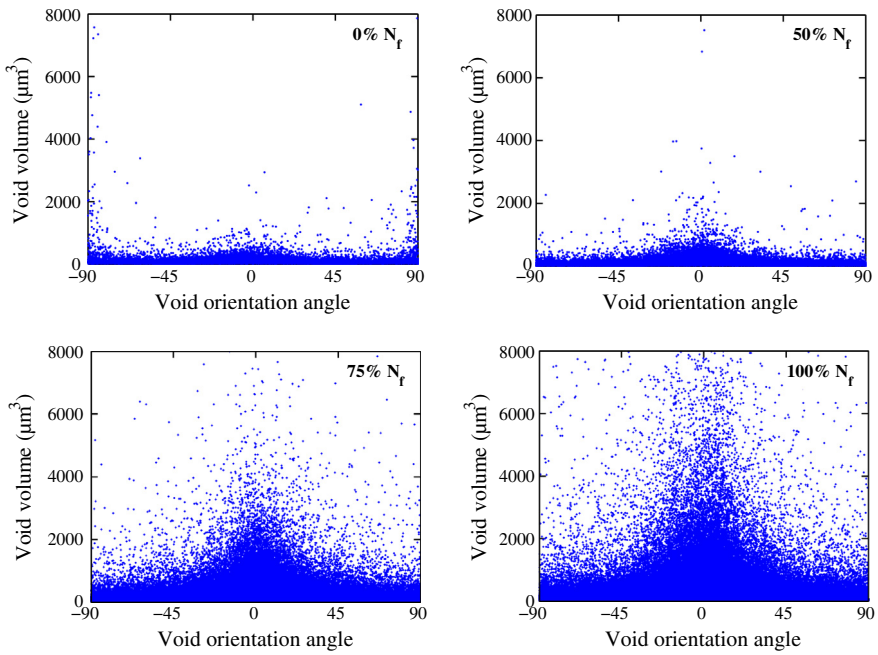

Fig. 22. Void orientation angle vs. void volume graphs of the upper shell layer of longitudinal specimens that have been fatigue loaded up to several percentages of fatigue life (N_f) at maximum stress level of 60% σ_u.

fibers. However, it is difficult to quantify the degree of interfacial debonding as the fiber length is not unique. Indeed, fiber length variability is developed due to the injection process. Matrix microcracks at high stress level have been observed but do not seems to be dominant in the damage process for dry as molded PA66/GF30.

6. Concluding remarks

The macroscopic and microscopic fatigue damage behavior of PA66/GF30 have been studied. The experimental results related to the evolution of dynamic modulus, strain, temperature and energy dissipation are important to evaluate the damage evolution. The dynamic modulus can be used as a damage indicator, though in high stress level it may overpredict the damage evolution due to the high viscous effect contribution of the composite.

Based on thermography analysis on PA66/GF30 surface, diffuse damage occurs over the entire specimen. However, the microscopic observation by μCT technique states that the diffuse damage does not necessarily exhibit the same level between different locations inside the specimen.

The μCT analysis shows that the damage is mainly developed along fiber interface in the form of fiber/matrix interfacial debonding, except at the core layer of transverse specimen where matrix microcrack with preferential direction transversely to the applied load is dominant due to the locally high stress concentration.

The μCT results also demonstrate that the damage continuously increases during fatigue loading. However, the damage evolution occurs more significantly in the second half of the fatigue life. Despite high resolutions used in this work, detection of fiber/matrix interfacial debonding in the early stages of fatigue life was difficult. Observation with higher resolution is then required to further investigate these early stages.

The observed damage mechanisms and evolution are currently integrated into a micromechanical modeling in order to propose a physically based, microstructure dependent fatigue model. Further work on spatial damage distribution by μCT analysis is underway and will be presented in a forthcoming paper.

References

[1] Horst JJ, Spoormaker JL. Mechanisms of fatigue in short glass fiber reinforced polyamide 6. Polym Eng Sci 1996;36(22):2718–26.
[2] Horst JJ, Spoormaker JL. Fatigue fracture mechanisms and fractography of short-glassfibre-reinforced polyamide 6. J Mater Sci 1997;32(14):3641–51.
[3] Ben Cheikh Larbi A, Sai K, Sidhom H, Baptiste D. Constitutive model of micromechanical damage to predict reduction in stiffness of a fatigued SMC composite. J Mater Eng Perform 2006;15(5):575–80.

[4] Toubal L, Karama M, Lorrain B. Damage evolution and infrared thermography in woven composite laminates under fatigue loading. Int J Fatigue 2006;28(12):1867–72.
[5] Mourglia-Seignobos E. Compréhension des mécanismes physiques de fatigue dans le polyamide vierge et renforcé de fibres de verre. Ph.D. thesis; INSA Lyon; 2009.
[6] Nouri H, Meraghni F, Lory P. Fatigue damage model for injection-molded short glass fibre reinforced thermoplastics. Int J Fatigue 2009;31(5):934–42.
[7] Meraghni F, Nouri H, Bourgeois N, Czarnota C, Lory P. Parameters identification of fatigue damage model for short glass fiber reinforced polyamide (PA6-GF30) using digital image correlation. Proc Eng 2011;10:2110–6.
[8] Nouri H, Czarnota C, Meraghni F. Experimental parameters identification of fatigue damage model for short glass fiber reinforced thermoplastics GFRP. In: Haddar M, Romdhane L, Louati J, Ben Amara A, editors. Design and modeling of mechanical systems. Lecture notes in mechanical engineering. Berlin, Heidelberg: Springer Berlin Heidelberg; 2013. p. 523–30.
[9] Steinberger R, Valadas Leitao TI, Ladstatter E, Pinter G, Billinger W, Lang RW. Infrared thermographic techniques for non-destructive damage characterization of carbon fibre reinforced polymers during tensile fatigue testing. Int J Fatigue 2006;28(10):1340–7.
[10] Ghorbel A, Saintier N, Dhiab A. Investigation of damage evolution in short glass fibers reinforced polyamide 6,6 under tensile loading using infrared thermography. Proc Eng 2011;10:2123–8.
[11] Esmaeillou B, Fitoussi J, Lucas A, Tcharkhtchi A. Multi-scale experimental analysis of the tension–tension fatigue behavior of a short glass fiber reinforced polyamide composite. Proc Eng 2011;10:2117–22.
[12] Esmaeillou B, Ferreira P, Bellenger V, Tcharkhtchi A. Fatigue behavior of polyamide 66/glass fiber under various kinds of applied load. Polym Compos 2012;33(4):540–7.
[13] Esmaeillou B, Fereirra P, Bellenger V, Tcharkhtchi A. Fatigue damage initiation of a PA66/glass fibers composite material. J Appl Polym Sci 2012;125(5):4007–14.
[14] Montesano J, Fawaz Z, Bougherara H. Use of infrared thermography to investigate the fatigue behavior of a carbon fiber reinforced polymer composite. Compos Struct 2013;97:76–83.
[15] Bayraktar E, Antolonovich S, Bathias C. Multiscale study of fatigue behaviour of composite materials by χ-rays computed tomography. Int J Fatigue 2006;28(10):1322–33.
[16] Lambert J, Chambers A, Sinclair I, Spearing S. 3D damage characterisation and the role of voids in the fatigue of wind turbine blade materials. Compos Sci Technol 2012;72(2):337–43.
[17] Withers PJ, Preuss M. Fatigue and damage in structural materials studied by X-ray tomography. Annu Rev Mater Res 2012;42(1):81–103.
[18] Cosmi F, Bernasconi A. Micro-CT investigation on fatigue damage evolution in short fibre reinforced polymers. Compos Sci Technol 2013;79:70–6.
[19] Arif MF, Meraghni F, Chemisky Y, Despringre N, Robert G. In situ damage mechanisms investigation of PA66/GF30 composite: effect of relative humidity. Compos Part B: Eng 2013(0).
[20] Mallick PK, Zhou Y. Effect of mean stress on the stress-controlled fatigue of a short E-glass fiber reinforced polyamide-6,6. Int J Fatigue 2004;26(9):941–6.
[21] Bernasconi A, Kulin RM. Effect of frequency upon fatigue strength of a short glass fiber reinforced polyamide 6: a superposition method based on cyclic creep parameters. Polym Compos 2009;30(2):154–61.
[22] Bernasconi A, Davoli P, Basile A, Filippi A. Effect of fibre orientation on the fatigue behaviour of a short glass fibre reinforced polyamide-6. Int J Fatigue 2007;29(2):199–208.
[23] Nouri H. Modélisation et identification de lois de comportement avec endommagement en fatigue polycyclique de matériaux composite a matrice thermoplastique. Ph.D. thesis; Arts et Métiers ParisTech; 2009.
[24] De Monte M, Moosbrugger E, Quaresimin M. Influence of temperature and thickness on the off-axis behaviour of short glass fibre reinforced polyamide 6.6 Quasi-static loading. Compos Part A: Appl Sci Manuf 2010;41(7):859–71.
[25] Klimkeit B, Castagnet S, Nadot Y, El Habib A, Benoit G, Bergamo S, et al. Fatigue damage mechanisms in short fiber reinforced PBT+PET GF30. Mater Sci Eng: A 2011;528(3):1577–88.
[26] ID19 ESRF. <http://www.esrf.eu/UsersAndScience/Experiments/Imaging/ID19>.
[27] Advani SG, Tucker CL. The use of tensors to describe and predict fiber orientation in short fiber composites. J Rheol 1987;31.
[28] Mlekusch B. Fibre orientation in short-fibre-reinforced thermoplastics II. Quantitative measurements by image analysis. Compos Sci Technol 1999;59:547–60.
[29] Eberhardt CN, Clarke A. Fibre-orientation measurements in short-glass-fibre composites. Part I: Automated, high-angular-resolution measurement by confocal microscopy. Compos Sci Technol 2001;61(10):1389–400.
[30] Lee Y, Lee S, Youn J, Chung K, Kang T. Characterization of fiber orientation in short fiber reinforced composites with an image processing technique. Mater Res Innovat 2002;6(2):65–72.
[31] Zhou Y, Mallick P. Fatigue performance of an injection-molded short E-glass fiber-reinforced polyamide 6,6. I. Effects of orientation, holes, and weld line. Polym Compos 2006;27(2):230–7.
[32] De Monte M, Moosbrugger E, Quaresimin M. Influence of temperature and thickness on the off-axis behaviour of short glass fibre reinforced polyamide 6.6 cyclic loading. Compos Part A: Appl Sci Manuf 2010;41(10):1368–79.
[33] Sonsino C, Moosbrugger E. Fatigue design of highly loaded short-glass-fibre reinforced polyamide parts in engine compartments. Int J Fatigue 2008;30(7):1279–88.
[34] Ladeveze P, Le Dantec E. Damage modelling of the elementary ply for laminated composites. Compos Sci Technol 1992;43(3):257–67.